GEOLOGY

Boutique neutrons advance $^{40}Ar/^{39}Ar$ geochronology

Daniel Rutte[1,2*†], Paul R. Renne[1,2], Jonathan Morrell[3], Liqiang Qi[4‡], Mauricio Ayllon[3,5], Karl van Bibber[3], Jonathan Wilson[4], Tim A. Becker[1], Jon Batchelder[3], Lee A. Bernstein[3,5], Mathieu Lebois[4], Jay James[3], Su-Ann Chong[3§], Will L. Heriot[3], Max Wallace[3], Angel Marcial[3], Charles Johnson[3], Graham Woolley[3], Parker A. Adams[3]

We designed and tested a compact deuteron-deuteron fusion neutron generator for application to $^{40}Ar/^{39}Ar$ geochronology. The nearly monoenergetic neutrons produced for sample irradiation are anticipated to provide several advantages compared with conventional fission spectrum neutrons: Reduction of collateral nuclear reactions increases age accuracy and precision. Irradiation parameters within the neutron generator are more controllable compared with fission reactors. Confidence in the prediction of recoil energies is improved, and their likely reduction potentially broadens applicability of the dating method to fine-grained materials without vacuum encapsulation. Resolution of variation in the $^{39}K(n,p)^{39}Ar$ neutron capture cross section at 1.3 to 3.2 MeV and discovery of a strong resonance at ~2.4 MeV illuminate future pathways to improve the technique for $^{40}Ar/^{39}Ar$ dating.

INTRODUCTION

Precise geochronology is the basis for quantification of processes in Earth and planetary sciences and allied fields such as archeology. The $^{40}Ar/^{39}Ar$ technique is the most versatile dating technique available in terms of the applicable age range and diversity of geological environments, having been used to date materials from the formation of our Moon ca. 4 billion years ago (*1*) to historically recorded volcanic eruptions (*2*). It is widely used, e.g., for dating of volcanic tephra in sedimentary sequences recording human evolution and climate variability (*3*), the timing and causes of biotic evolution and mass extinctions (*4*), and determination of exhumation rates in mountain belts (*5*). The rock clock is based on the natural radioactive decay of ^{40}K to $^{40}Ar^*$. The technique requires neutron irradiation of the sample to transmute ^{39}K via a neutron capture, proton emission (n,p) reaction to $^{39}Ar_K$, which is then a proxy for ^{40}K and allows the critical daughter/parent isotope ratio to be measured by noble gas mass spectrometry. After correction for Ar isotopes arising from air contamination and collateral reactions from the irradiation, the measured $^{40}Ar^*/^{39}Ar_K$ of a sample is converted to $^{40}Ar^*/^{40}K$ through geological age standards that are co-irradiated with samples. Conventionally, $^{40}Ar/^{39}Ar$ samples are irradiated in nuclear fission reactors providing a wide spectrum of neutron energies resulting in two limitations: (i) Kinetic energy of the neutron impact and proton emission is partially transferred to the produced ^{39}Ar, resulting in a recoil effect, its redistribution, and, potentially, ^{39}Ar loss. "Recoil" loss leading to erroneously old ages is significant for samples with large surface per volume, i.e., fine-grained materials and materials with significant volume of nonretentive sites (*6*). The effect was resolved for grain dimensions smaller than ~50 μm and results in inaccuracies up to ~20% for materials with grain sizes around 5 μm (*7*). This places materials such as calcium-aluminum–rich inclusions in meteorites (the oldest materials in the solar system), clay minerals, or volcanic glass shards (of interest in crystal free tephra) out of limits for accurate conventional $^{40}Ar/^{39}Ar$ dating. (ii) Multiple reactions induced by the broad spectrum of the neutrons in a reactor core produce Ar isotopes from K, Ca, and Cl (*8*) and mass interfering ^{80}Kr from Br (*9*), e.g., the reaction $^{42}Ca(n,n\alpha)^{36}Ar$. Here, the interfering reactions that create ^{36}Ar are the most critical as ^{36}Ar is used to determine the amount of atmospheric Ar in a sample and, accordingly, subtract the atmospheric ^{40}Ar from the total ^{40}Ar to determine the radiogenic component relevant for the age calculation. Because of an atmospheric $^{40}Ar/^{36}Ar$ ratio of 298.56 (*10*), uncertainty of the ^{36}Ar measurement propagates with more than two orders of magnitude into the age. Corrections for all known interfering reactions are possible, but significantly add to the uncertainty in ages (*11*). Besides undesired reactions, the production of ^{37}Ar via $^{40}Ca(n,\alpha)^{37}Ar$ and ^{38}Ar via $^{37}Cl(n,\gamma,\beta)^{38}Ar$ are useful tracers of Ca and Cl contents. They allow monitoring, e.g., the degassing composition of phases with Ca/K zonation or hydrous alteration through increased Cl contents. In the case of ^{36}Ar and ^{37}Ar produced from Ca, the intricacies of collateral reactions and recoil mingle: $^{37}Ar_{Ca}$ is used for the correction of $^{36}Ar_{Ca}$, but their production involving alpha and proton emission, respectively, result in a different recoil loss and a flawed $^{36}Ar_{Ca}$ correction, typically making the ages erroneously young (*12*, *13*).

Renne *et al.* (*11*) proposed to build a deuteron-deuteron (D-D) fusion neutron generator to produce quasi-monoenergetic neutrons of ~2.5 MeV [$D(D,n)^3He$]. Compared with fission neutrons, they anticipated it to reduce $^{39}Ar_K$ recoil ranges by a factor of 3 and exclude or minimize by energy threshold or small neutron cross section all undesired interference reactions while still allowing the production of ^{37}Ar as a valuable tracer for Ca (*11*). The reduction of $^{38}Ar_{Cl}$ production as a tracer for Cl, which is predicted to be about three orders of magnitude smaller than in fission reactors, relative to ^{39}Ar production from K (*14*), may be a disadvantage for some applications. Such a proposed apparatus, dubbed the high flux neutron generator (HFNG), has been constructed at the University of California (UC) Berkeley, commissioned in 2013, and has undergone continuous upgrades subsequently. Its design and technical capabilities were

[1]Berkeley Geochronology Center, Berkeley, CA 94709, USA. [2]Department of Earth and Planetary Sciences, University of California, Berkeley, Berkeley, CA 94720, USA. [3]Department of Nuclear Engineering, University of California, Berkeley, Berkeley, CA 94720, USA. [4]Institut de Physique Nucléaire d'Orsay, 91406 Orsay Cedex, France. [5]Lawrence Berkeley National Laboratory, Berkeley, CA 94720, USA.
*Corresponding author. Email: drutte@bgc.org
†Present address: Institut für Geowissenschaften, Universität Bonn, 53115 Bonn, Germany.
‡Present address: Key Laboratory for Particle Astrophysics, Institute of High Energy Physics, Beijing 100049, China.
§Present address: University of Tennessee, Knoxville, TN 37966, USA.

recently detailed in (*15*). Here, we report (i) the first dating and experiments to quantify (ii) the reduction of recoil, (iii) interference reactions, and (iv) the $^{39}K(n,p)^{39}Ar$ cross section at 1.3 to 3.2 MeV.

RESULTS

(i) To test our ability to date "unknowns," we co-irradiated the geological age standard Alder Creek sanidine [ACs; 1.1848 ± 0.0006 million years (Ma); uncertainties are 1σ throughout] (*16*), sanidine from the Campanian Ignimbrite [MDP-1; 39.85 ± 0.14 thousand years (ka)] (*17*), and sanidine from the 79 CE eruption of Vesuvius documented by Pliny the Younger (1.939 ka; AM-1). (ii) For a first-order quantification of recoil effects, we produced grain size fractions of MDP-1 ranging down to <15 μm by crushing and sieving pristine 180- to 300-μm crystals. (iii) To investigate production of collateral reactions on Ca and K, we irradiated CaF_2 and a glass with 11.3 weight % (wt %) K. (iv) In ancillary experiments, we determined the cross section of $^{39}K(n,p)^{39}Ar$ as a function of neutron energy. We used the capabilities of the HFNG to provide different neutron energies at different angles as a result of the two-body fusion reaction [~2.76 MeV forward-most to ~2.2 MeV backward; (*15*), with respect to the incident deuteron beam]. We expanded on this energy range by using the LICORNE (Lithium Inverse Cinematic ORsay NEutron source) apparatus at the Accélérateur Linéaire et Tandem à Orsay (ALTO) facility of the Institut de Physique Nucléaire d'Orsay (IPN) that produces 0.5- to 4-MeV neutrons (*18*), based on the reaction $p(^7Li,n)^7Be$.

Dating, recoil, and interference reactions

We irradiated 2 to 5 mg of each sample in wells arranged in a triangular pattern over an area of 12 mm by 10 mm with 12 aliquots of a 180- to 300-μm control fraction of MDP-1, bracketing and interleaving the other samples to monitor for ^{39}Ar production rate variation (Fig. 1). *F* values ($^{40}Ar^*/^{39}Ar_K$) of the dispersed 180- to 300-μm fractions indicate little variation in $^{39}Ar_K$ production rate in the central sample array (Fig. 1). Only the *F* value of the sample in marginal hole 17 differs from the other holes outside uncertainty at the 2σ level. The ratios of *F* values (*R* values) (*19*) of the different samples are an independent measure of relative age; they are given in table S2 and are concordant with reported literature values. Using MDP-1 as the geological age standard, we calculate inverse variance–weighted mean ages of 1.183 ± 0.046 Ma for ACs and 2.3 ± 1.1 ka for AM-1.

To test for recoil loss of ^{39}Ar through grain surfaces, we normalized *F* values of the fine-grained fractions of MDP-1 with the *F* values of the surrounding control fraction aliquots (Figs. 1 and 2). Deviation of the normalized *F* value from unity is equivalent to the age bias caused by ^{39}Ar recoil loss. A similar approach was used by Jourdan *et al.* (*12*), who analyzed different grain sizes of sanidine and a sanidine and plagioclase mixture, and by Paine *et al.* (*7*), who analyzed individual platy grains of biotite of different thicknesses. For comparability, we calculated surface area per volume (SAV) ratios of individual grains and fractions, assuming cube and cylinder shapes for sanidine and biotite, respectively. Jourdan *et al.* (*12*) found a positive age bias for sanidine fractions <40 μm (SAV larger than ~0.1 μm^{-1}), which they interpreted as being due to ^{39}Ar recoil loss, and a negative age bias for the sanidine and plagioclase mixed fractions <40 μm, which they interpreted to result from undercorrection of $^{36}Ar_{Ca}$ because the tracer $^{37}Ar_{Ca}$ experienced relatively more recoil loss (Fig. 2A). Paine *et al.* (*7*) found a positive age bias for grains with SAV >0.08 μm^{-1} interpreted as $^{39}Ar_K$ recoil loss. While uncertainties are comparably higher in our experiment, all our grain size fractions yielded *F* values of unity within uncertainty, indicating irresolvable recoil effects for ~2.75-MeV neutrons in this experiment.

To quantify the production of Ar isotopes from Ca and K, we analyzed three samples of CaF_2 and K-rich glass each. As desired, the production of the short-lived ^{37}Ar ($T_{1/2}$ = 34.95 ± 0.04 days) (*20*) is well quantifiable: The inverse variance–weighted mean production rate ratio of $^{37}Ar_{Ca}/^{39}Ar_K$ per Ca/K weight ratio is 0.249 ± 0.011, compared with a production rate ratio in fission reactors around 0.5. This confirms the usefulness of $^{37}Ar_{Ca}$ as a tracer of Ca content using D-D fission neutrons for irradiation. From CaF_2 analyses, we determined inverse variance–weighted $^{40}Ar/^{36}Ar$, $^{38}Ar/^{36}Ar$, and $^{39}Ar/^{37}Ar$ ratios of 299.3 ± 2.3, 0.189 ± 0.027, and 0.005 ± 0.012, which are indistinguishable from atmospheric values of 298.56 ± 0.31, 0.1885 ± 0.0003, and 0, respectively (*10*). This indicates no resolvable production of ^{40}Ar, ^{39}Ar, ^{38}Ar, and ^{36}Ar from Ca. Similarly, no quantifiable production of ^{40}Ar from K via $^{40}K(n,p)^{40}Ar$ could be resolved from the K-rich glass that provides an inverse variance–weighted mean $^{40}Ar_K/^{39}Ar_K$ production rate ratio of 0.8 ± 6.4.

$^{39}K(n,p)^{39}Ar$ cross section

We co-irradiated K-bearing targets (KBr- or K-rich glass) and metallic neutron fluence monitors (In or Ni foil) with neutrons of different energies. Following irradiation, the K-bearing target was analyzed for its ^{39}Ar content and the metallic neutron fluence monitors for their γ activity. Cross sections of the reaction $^{39}K(n,p)^{39}Ar$ were calculated against well-known cross sections of neutron-absorption reactions on In and Ni.

Our new cross section data resolve structure in the energy range of 1.3 to 3.2 MeV that has not been previously described (Fig. 3 and

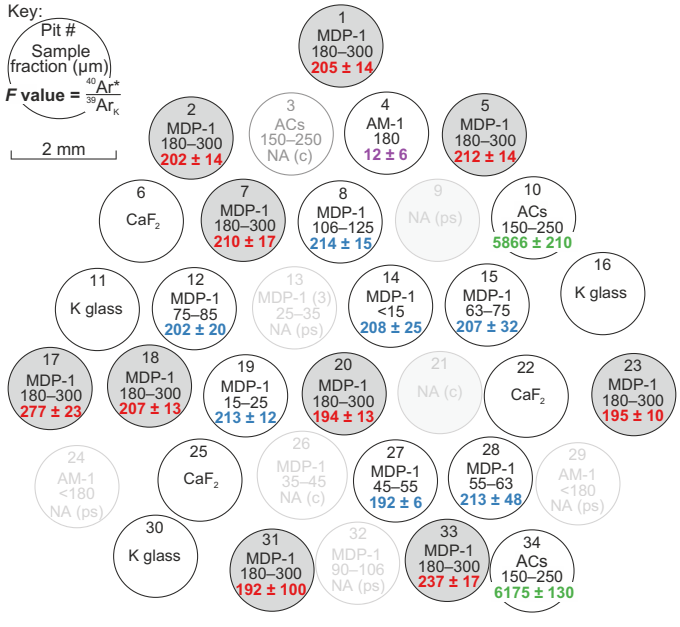

Fig. 1. Map of the sample holder used for the main HFNG experiment showing determined *F* values. Dark gray fields are the MDP-1 control samples to monitor production rate variations. Transparent holes are not-available (NA) analyses (NA). ps indicates peak suppression; c, accidental contamination. *F* values are in sample-specific colors for ease of orientation. Figure S1 provides a photograph of the actual sample holder.

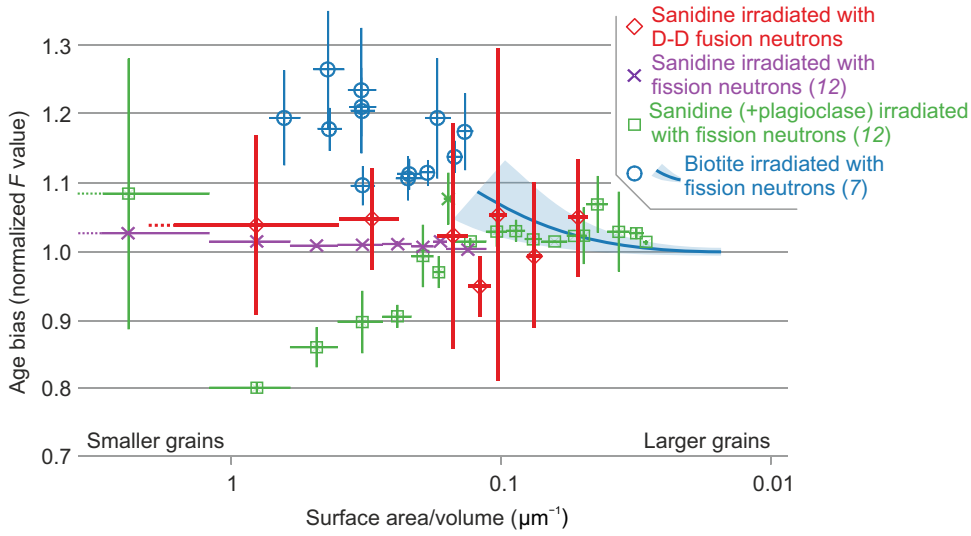

Fig. 2. $^{40}Ar/^{39}Ar$ age bias as a function of grain geometry for D-D fusion neutron or fission neutron–irradiated minerals. Positive age bias of high SAV biotite grains irradiated with fission neutrons is interpreted to represent recoil-related ^{39}Ar loss [data points are partially shown as means and envelope only; (*7*)]. Negative age bias of a sanidine-plagioclase mixture is interpreted to reflect undercorrection of $^{36}Ar_{Ca}$ (*12*). Biotite grains (*7*) were irradiated separately, while sanidine fractions [this study and (*12*)] were irradiated with multiple grains in contact, allowing potential reimplantation and decreasing apparent recoil.

Table 1). The cross section of the $^{39}K(n,p)^{39}Ar$ reaction shows nonstatistical behavior with variability exceeding a factor of 5 over <0.2 MeV. The experiments in the HFNG with an energy resolution around 0.02 MeV resolve this variability in detail in the range of 2.4 to 2.8 MeV. The LICORNE data with a generally coarser energy resolution suggest a nonsmooth function down to energies ~1.5 MeV: The cross section determined for ~1.46 MeV with a narrower neutron energy spectrum is higher than the cross section with a wider neutron energy spectrum averaging ~1.54 MeV (Fig. 3 and Table 1).

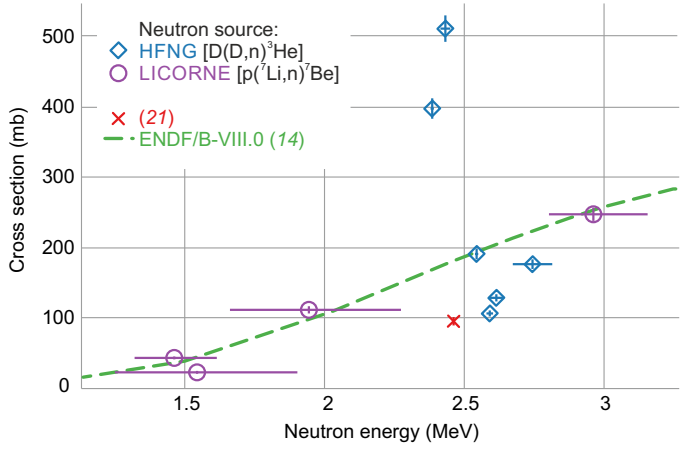

Fig. 3. Experimental cross section of the reaction $^{39}K(n,p)^{39}Ar$ as a function of neutron energy and their comparison with the most recent ENDF evaluation. Based on this study, (*34*) and (*14*). Error bars in neutron energy represent 67% limits of the neutron energy spectrum; error bars in the cross section represent analytical uncertainty. The strong variability in the cross section offers the possibility to magnify ^{39}Ar production rates by choosing the right neutron energy. ENDF, Evaluated Nuclear Data File.

DISCUSSION

Dating

The aliquots of the control fraction of sample MDP-1 in 10 holes display little spatial variation in *F* value ($^{39}Ar_K$ production rate) outside uncertainty with one exception (Fig. 1). The *F* value of hole 17 exceeds the average by 25% and outside 2σ uncertainty. We can only speculate on the reasons: Most likely, a grain of the neighboring K-rich glass contaminated this sample unnoticed. Hole 17 aside, our experiment shows that the setup used with a multi-aperture extraction plate can create $^{39}Ar_K$ production rates that vary in the single-digit percent range over >4 cm^2. This is on the higher side of gradients commonly observed in fission reactors (*21*) but sufficient for high-precision $^{40}Ar/^{39}Ar$ geochronology.

The determined *R* values and calculated absolute ages of ACs, AM-1, and MDP-1 are concordant with literature values (table S2) and provide the proof of concept for dating samples using the HFNG. The larger age uncertainties of our one to four aliquots as compared with previous work from experiments with several dozen aliquots are a statistical effect and not representative of the ultimately higher precision and accuracy achievable with the HFNG. This ultimately higher accuracy of the HFNG is anticipated on the basis of avoiding or reducing the need for correction of interfering reactions, with the most significant being $^{42}Ca(n,n\alpha)^{36}Ar$ for high Ca/K samples (*11*).

Recoil

The potential effect of recoil on $^{40}Ar/^{39}Ar$ geochronology was first recognized by Turner and Cadogan (*22*). Subsequent studies contributed to the understanding and quantification of Ar recoil by either theoretical estimation or experimental studies of different grain sizes of one mineral separate or vacuum encapsulation of mineral grains. Onstott *et al.* (*23*) calculated a theoretical estimate of ^{39}Ar recoil ranges by calculating ^{39}Ar recoil energies based on a fission flux spectrum and a smoothed $^{39}Ar(n,p)^{39}Ar$ cross section function and by simulating the transport range of ^{39}Ar ions with the resulting energies in silicate glass. A caveat of such a theoretical estimate of recoil energies is its limited

Table 1. Summary of irradiations used to determine the cross section (σ) of $^{39}K(n,p)^{39}Ar$ in the energy range of 1.2 to 3.2 MeV.

No.	Target	Neutron source	Energy (MeV)	Duration (hours)	^{39}K (mol)	Monitor reaction	Monitor σ (mb)*	Fluence (cm^{-2} s^{-1})	^{39}Ar (mol)	$^{39}K(n,p)$ σ (mb)
1	KBr	HFNG	2.75 ± 0.02	6.1	2.010 ± 0.001 × 10^{-3}	$^{115}In(n,n')^{115m}In$	345 ± 10	2.90 ± 0.104 × 10^{11}	1.03 ± 0.010 × 10^{-16}	177 ± 7
2a	KBr	LICORNE	2.96 (+0.19/−0.16)	6.0	9.6383 ± 0.0048 × 10^{-3}	$^{115}In(n,n')^{115m}In$	293 ± 12	2.08 ± 0.075E × 10^{10}	4.99 ± 0.051 × 10^{-17}	249 ± 9
2b	KBr	LICORNE	1.46 (+0.15/−0.14)	9.4	9.6005 ± 0.0048 × 10^{-3}	$^{115}In(n,n')^{115m}In$	163.1 ± 6.5	3.83 ± 0.14 × 10^{10}	1.61 ± 0.027 × 10^{-17}	44 ± 2
2c	KBr	LICORNE	1.54 (+0.36/−0.29)	18.4	9.3352 ± 0.0046 × 10^{-3}	$^{115}In(n,n')^{115m}In$	184.4 ± 7.4	4.72 ± 0.17 × 10^{10}	1.00 ± 0.029 × 10^{-17}	23 ± 1
2d	KBr	LICORNE	1.94 (+0.33/−0.28)	15.2	9.4607 ± 0.0047 × 10^{-3}	$^{115}In(n,n')^{115m}In$	213.3 ± 8.5	2.10 ± 0.076 × 10^{10}	2.24 ± 0.038 × 10^{-17}	112 ± 4
3b	K glass	HFNG	2.589 ± 0.011	210.2	5.1211 ± 0.0013 × 10^{-5}	$^{58}Ni(n,p)^{58}Co$	124.7 ± 9.4	7.55 ± 0.27 × 10^{12}	4.17 ± 0.049 × 10^{-17}	108 ± 4
3c	K glass	HFNG	2.613 ± 0.024	210.2	1.2366 ± 0.0003 × 10^{-4}	$^{58}Ni(n,p)^{58}Co$	128.6 ± 9.4	3.31 ± 0.12 × 10^{12}	5.30 ± 0.058 × 10^{-17}	130 ± 5
3d	K glass	HFNG	2.542 ± 0.007	210.2	2.0614 ± 0.0005 × 10^{-4}	$^{58}Ni(n,p)^{58}Co$	116.9 ± 9.7	5.37 ± 0.19 × 10^{11}	2.12 ± 0.032 × 10^{-17}	191 ± 7
3e	K glass	HFNG	2.431 ± 0.017	210.2	2.9220 ± 0. 0008 × 10^{-4}	$^{58}Ni(n,p)^{58}Co$	100.6 ± 7.6	5.67 ± 0.20 × 10^{11}	8.49 ± 0.094 × 10^{-17}	512 ± 19
3f	K glass	HFNG	2.382 ± 0.007	210.2	2.0153 ± 0.0005 × 10^{-4}	$^{58}Ni(n,p)^{58}Co$	94.4 ± 7.5	1.59 ± 0.057 × 10^{12}	1.28 ± 0.013 × 10^{-16}	399 ± 15

*Based on the simulated neutron spectra (Fig. 5) and cross section data from (*21*).

transferability because the neutron flux spectrum is an important input to the calculation, but is specific to reactor and irradiation position, varies over time, and is not a smooth function, because cross section functions of moderating materials are not necessarily smooth [cf. Figure 1 of (*21*) for a simulated neutron spectrum for a $^{40}Ar/^{39}Ar$ irradiation position]. While neutron moderation will generally decrease recoil energies, it is difficult to accurately predict how the complex structure of the $^{39}K(n,p)^{39}Ar$ cross section function affects the resulting average recoil energies when it is convolved with a complex neutron energy spectrum. In any case, we estimate ^{39}Ar recoil reduction with D-D neutrons by comparing ~2.7 MeV with the average neutron energy in fission reactors performing the $^{39}K(n,p)^{39}Ar$ reaction, which is the average of the convolution of the neutron energy flux spectrum and the $^{39}K(n,p)^{39}Ar$ cross section. This is relevant because the recoil of ^{39}Ar depends primarily on the energy of the neutron and, only to a much lesser extent, on the emission of the proton (*22*). We convolved the smoothed Evaluated Nuclear Data File (ENDF) cross section (*14*) with a Watt thermal fission flux spectrum and derived an average neutron energy of 4.1 MeV performing $^{39}K(n,p)^{39}Ar$. This suggests a reduction of average recoil energies by a factor of 0.65 when 2.7-MeV neutrons are used. The estimate of a reduction by a factor 0.3 by Renne *et al.* (*11*) was based on the erroneous assumption that calculations for a perfectly inelastic collision provide the maximum recoil energy. Our approach cannot capture the complexity in cross section structure and flux spectrum discussed above, nor can any approach until details of these features are resolved. Notably, average recoil energies are compared, which may oversimplify the complexity of loss and redistribution when recoil energies and, thus, recoil distances range over an order of magnitude (*23*). These caveats highlight the advantages of a quasi-monoenergetic neutron source that allows an accurate theoretical prediction of recoil energy and allows well-controlled experiments to test it.

The experimental approach to recoil quantification chosen in this study is to assess $^{40}Ar^*/^{39}Ar_K$ differences as a function of the grain SAV (*7*, *12*). This approach is regarded to mostly capture ^{39}Ar recoil loss through grain surfaces but may contain effects of loss from low-retentivity sites as a function of irradiation temperature or short circuit diffusion pathways that are grain size dependent (*12*). These processes are invoked by Jourdan *et al.* (*12*) to explain the difference between their sanidine data and the biotite data of Paine *et al.* (*7*) that indicate about a factor 5 more apparent recoil per SAV (Fig. 2). Another complicating factor is the reimplantation of recoiled ^{39}Ar into neighboring grains that makes the experiments difficult to compare: The biotite grains of Paine *et al.* (*7*) were separated by millimeter-thick aluminum, while in our experiment and the experiment of Jourdan *et al.* (*12*), multiple sanidine grains were irradiated in contact.

A more direct experimental approach is the vacuum encapsulation of samples during irradiation, in which recoiled ^{39}Ar is captured and can be analyzed separately. This method showed that clay minerals may lose ~30%; hornblende and biotite around 0.4%, but up to 1.2%; and sanidine 0.04 to 0.18% of the produced ^{39}Ar (*6*, *24*). Considering the grain geometries, these amounts exceed the expected recoil loss through surfaces and indicate mineral-dependent loss from nonretentive sites that, in many phases, exceeds loss from surface ejection (*6*, *24*).

Our experiment indicates that fine multigrain separates down to <15 μm can be irradiated without currently resolvable apparent ^{39}Ar recoil loss in the HFNG. It remains unclear how much reimplantation into neighboring grains contributes to this outcome. Our experiment, which was tailored around the current relatively low neutron flux capability of the HFNG, needs to be considered as a starting point for further investigation. Once the necessary neutron fluences can be achieved by the HFNG in acceptable irradiation time, experiments investigating Ar recoil from single encapsulated grains need to be carried out to quantify recoil loss through nonretentive sites and quantify possible reimplantation. These experiments can serve as a benchmark for simulation of recoil distances because the spectral character complicating the recoil energy calculation for fission spectrum neutrons becomes irrelevant.

Moreover, the HFNG's anisotropic neutron flux—sourcing from a disc-shaped region next to the samples—can allow previously inconceivable experiments such as the semidirectional neutron irradiation of grains with planar inhomogeneities (e.g., exsolutions) or advancement of implantation experiments [e.g., (*25*)] to determine oriented recoil distances. These could, for example, quantify phase-dependent recoil distance, test the effect of ^{39}Ar ion channeling, and improve our understanding of the degassing behavior of mixed phases.

Collateral reactions

Our analyses support the anticipated reduction of unwanted interference reactions from Ca and K while easily quantifiable amounts of $^{37}Ar_{Ca}$ are produced, thus retaining its use as a tracer. However, at the current production levels of the HFNG, even the production rate ratios known from fission reactors that are expected to be higher could not be resolved analytically. Further experiments with higher neutron flux are required to enable more precise quantification of the reduction with reasonable irradiation times. Rendering the correction of interfering reactions obsolete or reducing them does not only reduce uncertainty in ages but also ameliorate the differential recoil loss of $^{36}Ar_{Ca}$ and $^{37}Ar_{Ca}$, resulting in erroneous age corrections (*12*). The largely advantageous results of eliminating thermal neutrons in the HFNG come at the cost of losing the sometimes useful capability to produce noble gas isotopes from halogens, e.g., via ^{37}Cl(n,γ,β$^-$)^{38}Ar, that allows tracing aqueous alteration or fluid and melt inclusions (*26*). To overcome this drawback, a potential moderation of neutrons by using a 20 cm thick polyethylene sarcophagus encasing the HFNG is currently under testing. Initial results obtained by enclosing the instrument except for its bottom indicate a fast/thermal neutron flux ratio around 170, which would be sufficient for an $^{39}Ar_K/^{38}Ar_{Cl}$ production rate of 0.004. To be useful for tracing Cl, an $^{39}Ar_K/^{38}Ar_{Cl}$ production rate >1 would require a fast/thermal flux ratio of 0.6; however, other advantages of the HFNG would be lost. In principle, the instrument configuration could be tailored to whether or not the desirability of measuring $^{38}Ar_{Cl}$ outweighs the benefits of reducing the thermal neutron flux.

^{39}K(n,p)^{39}Ar cross section

Our new results resolve a complex structure in the ^{39}K(n,p)^{39}Ar cross section at 2.4 to 2.8 MeV and indicate additional complexity around 1.5 MeV. This is similar to a recently found resolved resonance region for the reaction ^{35}Cl(n,p)^{35}S in the same energy range (*27*) and is not entirely expected, given the low-level density in nuclei near the N,Z = 20 shell closure. This discovery informs future instrumental design to include ^{40}Ar/^{39}Ar sample irradiation capabilities at higher angle and, thus, lower neutron energy: A minimally threefold higher cross section at ~2.4 MeV (~112° at 100-keV D acceleration) results in higher production rates even if the neutron yield is at only 55% of the forward direction.

The resolved structure also has implications for fission reactors that require further quantification: The folding of a nonsmooth cross section function with a nonsmooth neutron spectrum that varies between and within reactors may explain variations observed in production rates that are commonly considered to be a result of neutron fluence gradients alone. We conclude that further experiments would be fruitful for elaborating the ^{39}K(n,p)^{39}Ar cross section in further detail.

Additional benefits

Compared to conventional fission neutron irradiation, the HFNG offers several advantages beyond the merits discussed above: (i) It allows for irradiation at about room temperature compared to temperatures of, for example, ~270°C determined for using Al disks as sample holders in CLICIT (cadmium-lined in-core irradiation tube), the most utilized irradiation facility for ^{40}Ar/^{39}Ar geochronology at the Oregon State University research reactor. This provides an opportunity to date thermally unstable phases and those prone to Ar diffusion at low temperatures. (ii) The HFNG provides reproducible irradiation conditions. (iii) It reduces production of radioactive waste and exposure of personnel to radiological hazards. (iv) As a small-scale facility, it provides independence from a shrinking pool of research reactors worldwide. (v) The cost of irradiation with the HFNG is expected to be lower compared to a fission reactor because costly safety and environmental aspects are absent or less complex. In addition, application of D-D neutrons to ^{21}Ne cosmic ray exposure dating offers promise for illuminating planetary surface processes (*28*).

CONCLUSIONS

We provide the proof of concept for using a D-D fusion neutron generator for an ^{40}Ar/^{39}Ar sample irradiation. We successfully reproduced

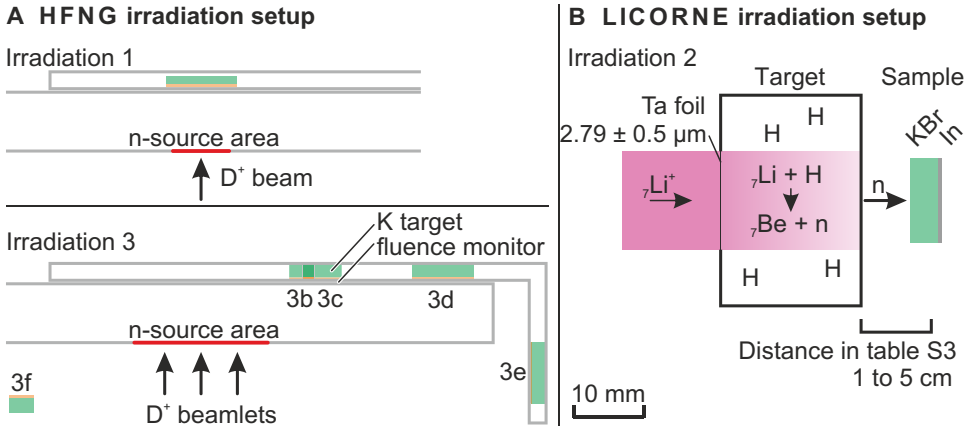

Fig. 4. Irradiation setup of neutron cross section experiments. (**A**) Geometry of samples in the HFNG with respect to the neutron source area where the D$^+$ beamlets impinge on the Ti layer hosting the interstitially implanted D. The neutron energy spectrum each target was exposed to is given in Fig. 5). (**B**) Setup of the LICORNE experiment and irradiation geometry. Table 1 and table S3 list the irradiation details.

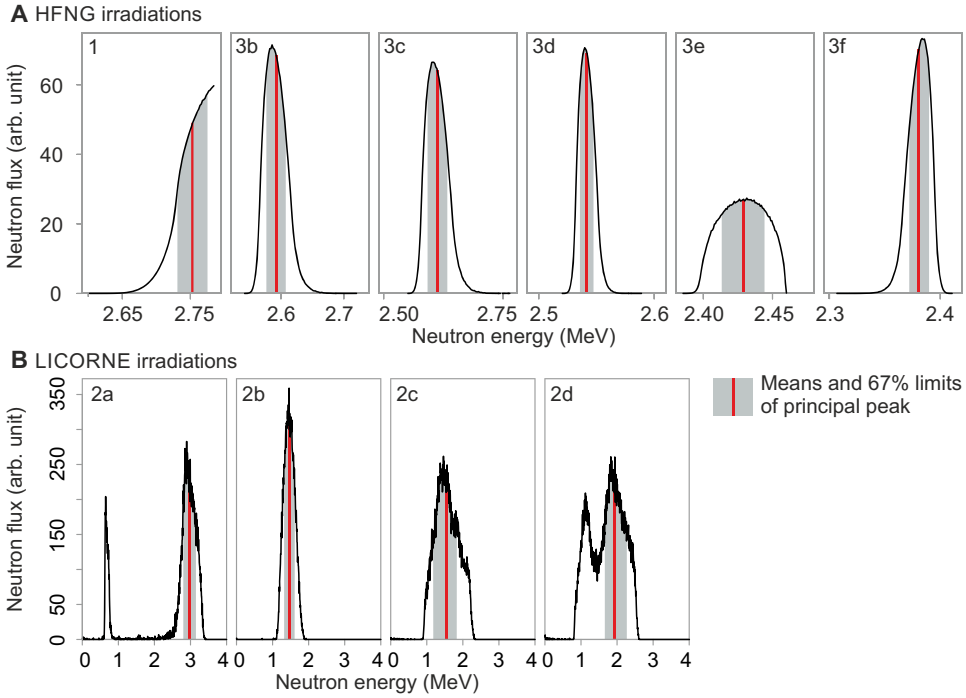

Fig. 5. Simulated neutron energy spectra of cross section experiments. (**A**) Neutron energy spectra of the six HFNG irradiation targets calculated using the MCNP. The spectra are a function of the radial distribution of the neutron beam, the energy-angle correlation of the neutron source, the intensity-angle correlation, and the solid angle. Table 1 lists the irradiation details. (**B**) Simulated neutron energy spectra of the four LICORNE-irradiated samples calculated. The spectra are a function of hydrogen cell target geometry, ^{7}Li energy, and solid angle covered by the sample. Table 1 and table S3 list the irradiation details.

the ages of three well-characterized samples ranging from 1.9 ka to 1.2 Ma. We find no grain size–dependent age bias for grain fractions down to <15 μm of a 40-ka sanidine from the Campanian Ignimbrite, supporting the anticipated reduction of ^{39}Ar recoil. This promising result requires further experimental quantification at increased neutron flux. A first quantification of interference reactions also supports the anticipated reduction of unwanted interference reactions, while the tracer reaction ^{40}Ca(n,α)^{37}Ar remains useful. In ancillary experiments, we resolve previously unrecognized structure in the ^{39}K(n,p)^{39}Ar cross section. Our results motivate further development of D-D fusion neutron generators for ^{40}Ar/^{39}Ar geochronology, with emphasis on increasing the ^{39}Ar production rate. This can be achieved by increasing the neutron flux and/or optimizing the design to exploit the newly found structure in the ^{39}K(n,p)^{39}Ar cross section.

MATERIALS AND METHODS

Irradiation and analysis of geological age standards, K-rich glass, and CaF_2

The geological age standards (MDP-1, AM-1, and ACs), CaF_2, and K-rich glass were loaded in a triangular drill pattern in an aluminum sheet. This sheet also held the samples of irradiation 3 described in the "Irradiation targets" section (Fig. 4). Figure 1 and fig. S1 show the sample array. After loading, the wells in the aluminum sheet were closed with aluminum foil and then sealed with Kapton tape. MDP-1 of the control fraction (180 to 300 μm; Fig. 1) bracketed AM-1, ACs, and MDP-1 of other grain size fractions to allow normalization of production rate variations over the sample array.

We used one ion source of the HFNG using a multi-aperture extraction plate, directing 31 beamlets of D^+ ions at a titanium surface 8 mm above the samples. Impinging with an energy of 100 keV, they produced neutrons through fusion with already embedded D (*15*). The setup resulted in a neutron source region with a diameter of 19 mm centered on the samples. The irradiation lasted 210.2 hours at an ~2.75-MeV neutron flux of ~2×10^7 n cm^{-2} s^{-1}. Quantified by the dimensionless irradiation parameter *J* used to characterize fission reactors (*29*), this translates to a *J*/hour of 5.2×10^{-10}, about six orders of magnitude below common fission neutron irradiation facilities. Following irradiation, the samples were transferred into a CO_2 laser extraction system and analyzed using mass spectrometry. We calculated inverse variance–weighted mean *F* values (^{40}Ar*/^{39}Ar$_K$) for each geological sample.

After irradiation, the front of the sample holder was opened hole by hole, and the material was moved—using a wetted paintbrush—onto weighing paper and, after drying and weighing (2 to 5 mg), was loaded into wells in a copper disk. On the basis of the weight and expected Ar signals, some samples were split into multiple aliquots (table S1). During the loading procedure, two samples were accidentally contaminated and discarded (Fig. 1).

The Ar was released from the samples by incremental heating using a CO_2 laser with a beam-shaping lense providing a flat energy profile of adjustable diameter. The released gas was purified for 300 s using a cold trap at −130°C to remove H_2O and a GP-50 SAES getter to remove reactive gases. After purification, the gas was allowed to expand into an Nu Instruments Noblesse 5 collector sector field noble gas mass spectrometer. Time series of ion beam intensities of Ar isotopes 36 through 40 were measured over 700 s and extrapolated to determine time-zero intercepts. We corrected for analysis blanks and mass spectrometer ion source mass discrimination. Radiogenic ^{40}Ar* was determined by subtraction of the atmospheric component

by subtracting ^{36}Ar multiplied by 298.56 (*30*). For the geological age standards, *F* values, i.e., $^{40}Ar^*/^{39}Ar_K$, were determined for each step. ^{37}Ar decay ($T_{1/2}$ = 34.95 ± 0.08 days) (*20*) in the analyzed CaF_2 was corrected for, accounting for decay during irradiation, irradiation breaks, and the time lag between irradiation and analysis. Uncertainties were linearly propagated. The largest source of uncertainty in the recoil experiment was the correction for air ^{40}Ar that amounted to ~90% of total ^{40}Ar in MDP-1. Analysis of five samples showed initially rising and strongly curved Ar isotope ion beam intensities. This observation is commonly interpreted to be an effect of contamination of the released Ar with other gases that are either inert or exceed the capabilities of the gas purification system, resulting in the initial suppression of Ar ionization (*9*). No meaningful time-zero intercepts could be determined for these samples, and they were discarded.

From the results of all heating steps of a sample, a weighted mean *F* value was determined (table S1). The weights were determined by inverse variance. To determine the *R* values (*19*) of MDP-1, ACs, and AM-1, we calculated the inverse variance–weighted mean *F* values of the MDP-1 samples of the control fraction surrounding the AC and AM-1 samples in the sample holder. Table S2 lists the *R* values (*19*) of the samples ACs, MDP-1, and AM-1 calculated from literature data given in the main text and compares them with the *R* values determined in this study (based on Fig. 1). They are indistinguishable within uncertainty.

Determination of ^{39}K(n,p)^{39}Ar cross section

Overview

To determine the cross section of ^{39}K(n,p)^{39}Ar, we irradiated a K-bearing material (KBr- or K-rich glass) along with a metallic neutron fluence monitor (In or Ni foil) with neutrons. We used two different reactions as a neutron source for energies ranging from 1.3 to 3.2 MeV: D-D fusion and p(^{7}Li,n)^{7}Be. Following irradiation, the K-bearing material was analyzed for its ^{39}Ar content, and the neutron fluence monitor was analyzed for its γ activity to calculate the neutron fluence. Cross sections of ^{39}K(n,p)^{39}Ar were then calculated against the well-known cross sections of neutron capture reactions on In and Ni.

Irradiation targets

We used KBr crystals and a K-rich glass (11.3 wt % K) as targets for the ^{39}K(n,p)^{39}Ar reaction. The merits of KBr are its comparably weak hygroscopic properties, stoichiometric and thus weighable and high K content, and commercial availability of high-purity large single crystals. The Ar retentiveness of KBr was ensured in an ancillary experiment by irradiation of KBr in a fission reactor, followed by stepwise degassing (*9*). For irradiation 1 (Table 1) in the HFNG, we used a cuboid target (10 mm by 10 mm by 1 mm) that was manufactured from a large single crystal, taking advantage of its perfect cleavage. The targets for LICORNE were unpolished cut disks (diameter, 12 mm; thickness, 4 mm) that were purchased through ISP Optics Corp. The KBr targets contained significant quantities of atmospheric Ar (~3×10^{-12} mol ^{40}Ar/g). To remove this atmospheric Ar before the irradiation, all targets were degassed at 450°C in ultrahigh vacuum (UHV; 2.7×10^{-6} Pa) for 24 hours. The targets were then removed from the furnace and exposed to atmosphere. One was reinserted and analyzed for its Ar content to ensure complete degassing. Insignificant atmospheric Ar was detected. The K-rich glass was acquired through Corning glass, broken and sieved. It was degassed in UHV to remove atmospheric Ar. We ensured homogeneity of the produced glass shards by electron microprobe analysis.

Neutron sources

High flux neutron generator. The HFNG is a prototype D-D fusion neutron generator developed at UC Berkeley's Department of Nuclear Engineering in collaboration with the Berkeley Geochronology Center. Deuterium was ionized in the plasma source by radio frequency excitation. It was then extracted through hole(s) in an extraction plate: Irradiation 1 used a single extraction hole with a diameter of 4 mm, while irradiation 3 used 31 holes with a diameter of 1 mm, arranged in a triangular pattern [cf. (*15*) for details on extraction plates]. The resulting beamlets were accelerated by a high-voltage differential potential (here 100 kV) and implanted in a Ti target. D^+ fuses with already implanted D to form ^{3}He with emission of a neutron. Technical details were recently reported by Ayllon *et al.* (*15*). For this experiment, we used its capabilities to provide different neutron energies with comparably high fluxes as a function of angle. The primary irradiation target (see the "Irradiation and analysis of geological age standards, K-rich glass, and CaF_2" section) was positioned 8 mm behind the fusion reaction interface and irradiated by neutrons emitted in the 0°, forward angle (laboratory frame) that have energies around 2.7 MeV (Fig. 4A). Secondary targets were positioned at various angles up to 113° (Fig. 4A) for which the neutrons range downward in energy to ~2.4 MeV.

The neutron flux spectra were determined using an analytical model for the neutron source combined with a Monte Carlo neutron transport model. This approach was developed and benchmarked by Ayllon *et al.* (*15*). The analytical model of the neutron source was based on the well-characterized kinematics of the D(D,n)^{3}He fusion reaction, simulation of beam transport physics, and target interactions. It takes into account the effects of acceleration voltage, beam current, ion beam optics, and deuterium diffusion within the target. The neutron flux spectra of individual samples were calculated using a Monte Carlo N-particle (MCNP) transport code using a discretized form of the source function as an input to the model. Figure 5A shows the neutron energy spectra of the individual samples.

LICORNE. The LICORNE was operated at the ALTO facility of the IPN (*18*). The tandem particle accelerator produces an intense ^{7}Li beam (typically 100 to 200 nA) that is directed through a Ta foil (2.79 μm) into a 2 cm long hydrogen gas cell operated at a pressure of 0.15 MPa and a flow rate of 0.5 cm^3/s (*31*). There, the reaction p(^{7}Li,n)^{7}Be creates a cone of neutrons in the forward direction toward the sample. The energy of the neutrons and the maximum opening angle of the cone depend on the incident energy of the ^{7}Li. We used incident ^{7}Li energies of 15.8 to 17.5 MeV (measured before the Ta foil) to create neutrons of up to ~3.2 MeV. Ancillary to the main neutron energy, a satellite peak was created at a lower intensity and a lower energy of 0.7 to 0.9 MeV (*18*). It arises from the neutrons emitted "backward" in the center of the mass frame that are still moving forward in the laboratory frame. The two peaks were merged at a ^{7}Li energy of 15.8 MeV and started to diverge at increasing energies. Narrowing the solid angle covered by the sample, i.e., the distance, was the main variable to narrow the full width half maximum of the main neutron spectrum (table S3). The limitations are the resulting lower neutron flux and the necessity to produce a well-quantifiable amount of ^{39}Ar. To optimize separation of primary and satellite peak and neutron flux, we placed the samples at varying distances of 1 to 5 cm behind the hydrogen gas cell (Fig. 4B and table S3). We tested for the influence of the satellite peak on the total ^{39}Ar activation by folding the neutron spectra with the latest ENDF ^{39}K(n,p)^{39}Ar cross section (*14*) and found it to be in or below the per mille range.

Direct measurements of the neutron spectrum close to the LICORNE inverse kinematics source are difficult because of the complex way in which the neutron spectrum and flux vary in three-dimensional space. The exact energy spectrum at a particular position, thus, needs to be calculated via Monte Carlo simulations, which must be validated by a direct measurement of the neutron spectrum at 0° using the time-of-flight (TOF) technique. We used a code based on the Geant4 Monte Carlo package that was developed for LICORNE to calculate the neutron spectrum received by each sample as a function of ^{7}Li energy and distance from the gas cell. The model has been validated in previous experiments (*18*) and verified by repeated TOF measurements using an EDEN scintillation detector module (*32*) at 3-m distance from the hydrogen gas cell the day before starting the reported irradiation experiments. Pulsing and bunching the ^{7}Li beam at 400-ns intervals allowed measurement of the TOF of the neutrons relative to the gamma peak [repetition of experiment described in (*18*)].

Neutron fluence determination

The neutron fluence received by the irradiation targets was determined using co-irradiated In or Ni foils, making use of the reactions ^{115}In(n,n′)^{115m}In and ^{58}Ni(n,p)^{58}Co as neutron fluence dosimeters. The foils covered the same solid angle as the target. After the end of irradiation, the 336-keV gammas from the decay of ^{115m}In and 811-keV gammas from the decay of ^{58}Co in the foil were measured using an HPGe (high-purity germanium) detector at ~10-cm sample detector separation. The detector was calibrated using ^{152}Eu and ^{133}Ba sources certified to 1.5% accuracy. Decay during irradiation and delay between irradiation and during the measurement were corrected for.

We calculated the ^{115}In(n,n')^{115m}In and ^{58}Ni(n,p)^{58}Co cross sections for each sample by folding the simulated neutron spectrum (Fig. 5) with interpolated cross section functions (*14*). The derived cross sections are given in Table 1.

Both LICORNE and HFNG exhibit fluctuations in neutron flux over the course of a multihour experiment. In LICORNE, these resulted primarily from inhomogeneity of the ^{7}Li source, requiring retuning of the ion source every few hours. In the HFNG, the loading of the deuterium in the Ti getter on the surface of the cathode results in a ramping up of the neutron flux over the first ~1.5 hours of the experiment, while the neutron flux can also vary throughout a run when ion source parameters are tuned to maximize efficiency. The 4.5-hour half-life of the ^{115m}In made monitoring of these fluctuations a necessity: The weight of each time increment of the irradiation experiment on the final activity of the monitor material is based on the half-life of the activation product and irradiation time. As a simple example, for a 4.5-hour irradiation, the contribution of the first time increment on the final ^{115m}In activity will be half of the contribution of the last increment because 50% of the isotopes produced during the first increment of the irradiation have already decayed by the end of the irradiation. For the LICORNE irradiation, we used an EDEN scintillation detector module (*32*), and for the HFNG irradiation, a Bonner sphere to monitor relative neutron flux fluctuations. Equation 1 represents a correction factor R, where A is the arithmetic mean of the measure of neutron flux (e.g., counts), λ is the decay constant of the produced isotope, t_n is the irradiation time, and x_i is a measure of neutron flux at any time increment.

$$R = \frac{A\sum_{i=0}^{n} e^{-\lambda(t_n - t_i)}}{\sum_{i=0}^{n} e^{-\lambda(t_n - t_i)}\chi_i} \quad (1)$$

As an example, fig. S2 shows the recorded time series of the Bonners sphere readback of irradiation 1 (Table 1) in the HFNG and the weight each time increment has in the calculation of the fluence from the In foil. A few-minute-long interruption toward the end of the irradiation evens out the initial phase where the flux is ramping up, resulting in a correction factor R of 0.99. Reported fluences in Table 1 include the correction factors. No such correction was necessary for the Ni foil where the half-life of 71 days was long compared to the irradiation length.

Analysis of ^{39}Ar contents of KBr- and K-rich glass

To release the ^{39}Ar for mass spectrometry, the KBr was fused in a resistance furnace and the K-rich glass was fused using a CO_2 laser. The released gas was purified and analyzed following procedures described in (*16*) for the Noblesse noble gas mass spectrometer. The sensitivity of the instrument was determined by analysis of the known radiogenic ^{40}Ar content of weighed aliquots of standards GA1550 and HD-B1 (*33*) before, during, and after analysis of the unknown samples. The sensitivity did not vary over the course of the measurements, and a mean value was determined. Expansion volumes were used to reduce Ar concentrations for the standards, but not for the unknown samples with smaller Ar contents. The relative volumes of furnace, laser cell, and expansion volumes were calibrated using repeated expansion and analysis of small aliquots of atmosphere. The difference in sensitivity between KBr- and K-rich glass analyses (Table 1) is related to the addition of the furnace volume for the KBr analyses. Uncertainties related to the radiogenic ^{40}Ar content of the standards (~0.8%), their weighing (~0.1%), volume calibration (~0.5%), and analysis (~0.1%) contribute to uncertainty of the sensitivity.

SUPPLEMENTARY MATERIALS

Supplementary material for this article is available at http://advances.sciencemag.org/cgi/content/full/5/9/eaaw5526/DC1

Fig. S1. Photograph of the sample holder after loading all samples but the <15-μm fraction of MDP-1.

Fig. S2. Impact and correction of neutron flux fluctuation biasing the determined average neutron fluence.

Table S1. Results of noble gas mass spectrometric analysis of geological age standards, K-rich glass and CaF_2.

Table S2. Comparison of R values based on literature data cited in the main text and this study.

Table S3. Irradiation details of LICORNE irradiations.

REFERENCES AND NOTES

1. G. Turner, Argon-40/argon-39 dating of lunar rock samples. *Science* **167**, 466–468 (1970).
2. P. R. Renne, W. D. Sharp, A. L. Deino, G. Orsi, L. Civetta, ^{40}Ar/^{39}Ar dating into the historical realm: Calibration against pliny the younger. *Science* **277**, 1279–1280 (1997).
3. D. J. Lowe, Tephrochronology and its application: A review. *Quat. Geochronol.* **6**, 107–153 (2011).
4. P. R. Renne, C. J. Sprain, M. A. Richards, S. Self, L. Vanderkluysen, K. Pande, State shift in Deccan volcanism at the Cretaceous-Paleogene boundary, possibly induced by impact. *Science* **350**, 76–78 (2015).
5. P. Copeland, T. M. Harrison, W. S. F. Kidd, X. Ronghua, Z. Yuquan, Rapid early Miocene acceleration of uplift in the Gangdese Belt, Xizang (southern Tibet), and its bearing on accommodation mechanisms of the India-Asia collision. *Earth Planet. Sci. Lett.* **86**, 240–252 (1987).
6. H. Dong, C. M. Hall, D. R. Peacor, A. N. Halliday, Mechanisms of argon retention in clays revealed by laser ^{40}Ar-^{39}Ar dating. *Science* **267**, 355–359 (1995).
7. J. H. Paine, S. Nomade, P. R. Renne, Quantification of ^{39}Ar recoil ejection from GA1550 biotite during neutron irradiation as a function of grain dimensions. *Geochim. Cosmochim. Acta* **70**, 1507–1517 (2006).
8. G. Turner, Argon 40-argon 39 dating: The optimization of irradiation parameters. *Earth Planet. Sci. Lett.* **10**, 227–234 (1971).
9. D. Rutte, T. A. Becker, P. R. Renne, Quantifying interference of krypton produced from neutron irradiation of inclusion-hosted and lattice-coordinated bromine with ^{40}Ar/^{39}Ar geochronology. *Geochim. Cosmochim. Acta* **211**, 1–9 (2017).

10. J.-Y. Lee, K. Marti, J. P. Severinghaus, K. Kawamura, H.-S. Yoo, J. B. Lee, J. S. Kim, A redetermination of the isotopic abundances of atmospheric Ar. *Geochim. Cosmochim. Acta* **70**, 4507–4512 (2006).
11. P. R. Renne, K. B. Knight, S. Nomade, K.-N. Leung, T.-P. Lou, Application of deuteron–deuteron (D–D) fusion neutrons to $^{40}Ar/^{39}Ar$ geochronology. *Appl. Radiat. Isot.* **62**, 25–32 (2005).
12. F. Jourdan, J. P. Matzel, P. R. Renne, ^{39}Ar and ^{37}Ar recoil loss during neutron irradiation of sanidine and plagioclase. *Geochim. Cosmochim. Acta* **71**, 2791–2808 (2007).
13. A. A. P. Koppers, H. Staudigel, J. R. Wijbrans, Dating crystalline groundmass separates of altered Cretaceous seamount basalts by the $^{40}Ar/^{39}Ar$ incremental heating technique. *Chem. Geol.* **166**, 139–158 (2000).
14. D. A. Brown, M. B. Chadwick, R. Capote, A. C. Kahler, A. Trkov, M. W. Herman, A. A. Sonzogni, Y. Danon, A. D. Carlson, M. Dunn, D. L. Smith, G.-M. Hale, G. Arbanas, R. Arcilla, C.-R. Bates, B. Beck, B. Becker, F. Brown, R. J. Casperson, J. Conlin, D. E. Cullen, M.-A. Descalle, R. Firestone, T. Gaines, K. H. Guber, A. I. Hawari, J. Holmes, T. D. Johnson, T. Kawano, B. C. Kiedrowski, A. J. Koning, S. Kopecky, L. Leal, J. P. Lestone, C. Lubitz, J. I. Márquez Damián, C. M. Mattoon, E. A. McCutchan, S. Mughabghab, P. Navratil, D. Neudecker, G. P. A. Nobre, G. Noguere, M. Paris, M. T. Pigni, A. J. Plompen, B. Pritychenko, V. G. Pronyaev, D. Roubtsov, D. Rochman, P. Romano, P. Schillebeeckx, S. Simakov, M. Sin, I. Sirakov, B. Sleaford, V. Sobes, E. S. Soukhovitskii, I. Stetcu, P. Talou, I. Thompson, S. van der Marck, L. Welser-Sherrill, D. Wiarda, M. White, J. L. Wormald, R. Q. Wright, M. Zerkle, G. Žerovnik, Y. Zhu, ENDF/B-VIII.0: The 8th major release of the nuclear reaction data library with CIELO-project cross sections, new standards and thermal scattering data. *Nuclear Data Sheets* **148**, 1–142 (2018).
15. M. Ayllon, P. A. Adams, J. D. Bauer, J. C. Batchelder, T. A. Becker, L. A. Bernstein, S.-A. Chong, J. James, L. E. Kirsch, K. Leung, E. F. Matthews, J. T. Morrell, P. R. Renne, A. M. Rogers, D. Rutte, A. S. Voyles, K. Van Bibber, C. S. Waltz, Design, construction, and characterization of a compact DD neutron generator designed for $^{40}Ar/^{39}Ar$ geochronology. *Nucl. Instrum. Methods Phys. Res. Sect. A Accel. Spectrom. Detect. Assoc. Equip.* **903**, 193–203 (2018).
16. E. M. Niespolo, D. Rutte, A. L. Deino, P. R. Renne, Intercalibration and age of the Alder Creek sanidine $^{40}Ar/^{39}$ Ar standard. *Quat. Geochronol.* **39**, 205–213 (2017).
17. B. Giaccio, I. Hajdas, R. Isaia, A. Deino, S. Nomade, High-precision ^{14}C and $^{40}Ar/^{39}Ar$ dating of the Campanian Ignimbrite (Y-5) reconciles the time-scales of climatic-cultural processes at 40 ka. *Sci. Rep.* **7**, 45940 (2017).
18. M. Lebois, J. N. Wilson, P. Halipré, B. Leniau, I. Matea, A. Oberstedt, S. Oberstedt, D. Verney, Development of a kinematically focused neutron source with the $p(^7Li,n)^7Be$ inverse reaction. *Nucl. Instrum. Methods Phys. Res. Sect. A* **735**, 145–151 (2014).
19. P. R. Renne, C. C. Swisher, A. L. Deino, D. B. Karner, T. L. Owens, D. J. DePaolo, Intercalibration of standards, absolute ages and uncertainties in $^{40}Ar/^{39}Ar$ dating. *Chem. Geol.* **145**, 117–152 (1998).
20. P. R. Renne, E. B. Norman, Determination of the half-life of ^{37}Ar by mass spectrometry. *Phys. Rev. C* **63**, 047302 (2001).
21. D. Rutte, J. A. Pfänder, M. Koleška, R. Jonckheere, S. Unterricker, Radial fast-neutron fluence gradients during rotating $^{40}Ar/^{39}Ar$ sample irradiation recorded with metallic fluence monitors and geological age standards. *Geochem. Geophys. Geosyst.* **16**, 336–345 (2015).
22. G. Turner, P. H. Cadogan, Possible effects of ^{39}Ar recoil in ^{40}Ar-^{39}Ar dating. *Proc. Fifth Lunar Conf.* **2**, 1601–1615 (1974).
23. T. C. Onstott, M. L. Miller, R. C. Ewing, G. W. Arnold, D. S. Walsh, Recoil refinements: Implications for the $^{40}Ar/^{39}Ar$ dating technique. *Geochim. Cosmochim. Acta* **59**, 1821–1834 (1995).
24. C. M. Hall, Direct measurement of recoil effects on $^{40}Ar/^{39}Ar$ standards. *Geol. Soc. Lond. Spec. Publ.* **378**, 53–62 (2014).
25. I. M. Villa, Direct determination of ^{39}Ar recoil distance. *Geochim. Cosmochim. Acta* **61**, 689–691 (1997).
26. S. Kelley, G. Turner, A. W. Butterfield, T. J. Shepherd, The source and significance of argon isotopes in fluid inclusions from areas of mineralization. *Earth Planet. Sci. Lett.* **79**, 303–318 (1986).
27. J. C. Batchelder, S.-A. Chong, J. Morrell, M. Unzueta, P. Adams, J. D. Bauer, T. Bailey, T. A. Becker, L. A. Bernstein, M. Fratoni, A. M. Hurst, J. James, A. M. Lewis, E. F. Matthews, M. Negus, D. Rutte, K. Song, K. Van Bibber, M. Wallace, C. S. Waltz, Possible evidence of non-statistical properties in the $^{35}Cl(n,p)^{35}S$ cross section. *Phys. Rev. C* **99**, 044612 (2019).
28. W. S. Cassata, An isochron approach to ^{21}Ne cosmic ray exposure dating by activation with deuteron-deuteron fusion neutrons. *Chem. Geol.* **284**, 21–25 (2011).
29. R. L. Grasty, J. G. Mitchell, Single sample potassium-argon ages using the omegatron. *Earth Planet. Sci. Lett.* **1**, 121–122 (1966).
30. S. Y. Park, J. S. Kim, J. B. Lee, M. B. Esler, R. S. Davis, R. I. Wielgosz, A redetermination of the argon content of air for buoyancy corrections in mass standard comparisons. *Metrologia* **41**, 387–395 (2004).
31. J. N. Wilson, M. Lebois, P. Halipre, S. Oberstedt, A. Oberstedt, The LICORNE neutron source and measurements of prompt γ-rays emitted in fission. *Phys. Procedia* **59**, 31–36 (2014).
32. H. Laurent, H. Lefort, D. Beaumel, Y. Blumenfeld, S. Fortier, S. Galès, J. Guillot, J. C. Roynette, P. Volkov, S. Brandenburg, EDEN: A neutron time-of-flight multidetector for decay studies of giant states. *Nucl. Instrum. Methods Phys. Res. Sect. A Accel. Spectrom. Detect. Assoc. Equip.* **326**, 517–525 (1993).
33. W. H. Schwarz, M. Trieloff, Intercalibration of ^{40}Ar-^{39}Ar age standards NL-25, HB3gr hornblende, GA1550, SB-3, HD-B1 biotite and BMus/2 muscovite. *Chem. Geol.* **242**, 218–231 (2007).
34. W. R. Dixon, J. H. Aitken, Absolute cross section of the $K^{39}(n,pp)A^{39}$ reaction for 2.5-MeV neutrons. *Nucl. Phys.* **24**, 456–464 (1961).

Acknowledgments: We acknowledge use of the ALTO facility, technical assistance by L. Morgan, and facilities support from the Ann and Gordon Getty Foundation. We thank C. Hall, A.A.P. Koppers, and two anonymous reviewers for the constructive criticism and K. Hodges for editorial handling. **Funding:** This research was funded by NSF grant EAR-0960138 (to P.R.R.), Deutsche Forschungsgemeinschaft (DFG; German Research Foundation) RU2065/1-1 (to D.R.), and U.S. DOE LBNL contract no. DE-AC02-05CH11231 (to L.A.B.). **Author contributions:** D.R., P.R.R., and T.A.B. designed the experiments. D.R., P.R.R., K.v.B., and L.A.B. acquired the funding. D.R., J.M., L.Q., M.A., J.B., J.J., S.-A.C., W.L.H., M.W., A.M., C.J., G.W., P.A.A., and H.M. operated the neutron sources. J.M. and L.Q. simulated the neutron energy spectra. D.R., J.M., and L.Q. performed the gamma spectrometry analysis. D.R. performed the noble gas analysis and evaluated the analytical data. D.R., J.M., and L.Q. developed the methodology and software. K.v.B., J.B., J.W., and M.L. managed the neutron sources. P.R.R., K.v.B., J.W., and M.L. oversaw the experiments. D.R. and J.M. visualized the results. D.R. wrote the original draft. All authors reviewed the manuscript. **Competing interests:** The authors declare that they have no competing interests. **Data and materials availability:** All data needed to evaluate the conclusions in the paper are present in the paper and/or the Supplementary Materials. Additional data related to this paper may be requested from the authors.

Submitted 4 January 2019
Accepted 8 August 2019
Published 11 September 2019
10.1126/sciadv.aaw5526

Citation: D. Rutte, P. R. Renne, J. Morrell, L. Qi, M. Ayllon, K. van Bibber, J. Wilson, T. A. Becker, J. Batchelder, L. A. Bernstein, M. Lebois, J. James, S.-A. Chong, W. L. Heriot, M. Wallace, A. Marcial, C. Johnson, G. Woolley, P. A. Adams, Boutique neutrons advance $^{40}Ar/^{39}Ar$ geochronology. *Sci. Adv.* **5**, eaaw5526 (2019).